Electronic Supplementary Information (ESI)

Ruthenium nanoparticles on covalent triazine frameworks incorporating thiophene for the electrocatalytic hydrogen evolution reaction

Lars Rademacher,[a] Thi Hai Yen Beglau,[a] Bahia Ali,[a] Linda Sondermann,[a] Till Strothmann,[a] István Boldog,[a] Juri Barthel,[b] Christoph Janiak[a,*]

Address:

[a] *Institut für Anorganische Chemie und Strukturchemie, Heinrich-Heine-Universität Düsseldorf, 40204 Düsseldorf, Germany*

[b] *Ernst Ruska-Zentrum für Mikroskopie und Spektroskopie mit Elektronen, Forschungszentrum Jülich GmbH, 52425 Jülich, Germany*

Emails:
lars.rademacher@hhu.de, beglau@hhu.de, bahia.ali@hhu.de, linda.sondermann@hhu.de, till.strothmann@hhu.de, boldogi@hhu.de, ju.barthel@fz-juelich.de, janiak@hhu.de

Contents

Materials

2,2'-Bithiophene-5,5'-dibromide (98%) and 2-thiophenecarbonitrile (99.98%) were obtained from BLD Pharm; 4-bromobenzonitrile (99%), palladium acetate, $Pd(OAc)_2$ (98%), tetrakis(triphenylphosphine)palladium, $Pd(PPh)_3$ (99%), and triruthenium dodecacarbonyl, $Ru_3(CO)_{12}$ (99%), from Sigma Aldrich; potassium acetate, KOAc (p.a.), and iron chloride hexahydrate, $FeCl_3x6H_2O$ (p.a.), from AppliChem; anhydrous potassium carbonate, K_2CO_3 (p.a.), and Toluol (p.a.) from Fisher Scientific; dimethylacetamide, DMA (99+%), and copper cyanide, CuCN (+99%), from Acros Organics; dimethylformamide, DMF (p.a.), from Honeywell, thiophene (99%) from Alfa Aesar. Water was purified with a Sartorius Arium Mini ultrapure water system.

Synthesis and characterization of the thiophene dinitrile CTF precursors

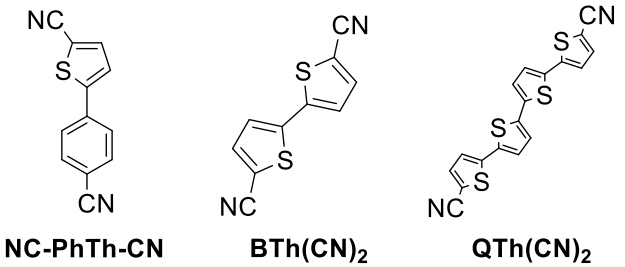

Fig. S1 Synthesized thiophene dinitrile CTF precursors.

5-(4-cyanophenyl)thiophene-2-carbonitrile (NC-PhTh-CN) was synthesized *via* a palladium-catalyzed C-H arylation, similarly to the literature.[1] 0.436 g (4.00 mmol) of 2-cyanothiophene, 0.364 g (2.00 mmol) of 4-bromobenzonitrile, 0.392 g (4 mmol) of KOAc, and 2 mg (0.009 mmol) of $Pd(OAc)_2$ were dissolved in 8 mL of dried DMA and stirred at 150 °C for 20 h. After cooling, 30 mL of water were added, and the mixture was extracted with 2×50 mL of dichloromethane. The organic phase was washed with 2×100 mL purified water and dried with $MgSO_4$. Column chromatography with cyclohexane / ethyl acetate (20:1 → 10:1) yields 0.315 g (75 %) of the yellow product.
^{1}H NMR (300 MHz, $CDCl_3$) δ (ppm): 7.64 (m, 4H), 7.57 (d, 4.0 Hz, 1H); 7.32 (d, 4.0 Hz, 1H); ^{13}C NMR (300 MHz, $CDCl_3$) δ (ppm): 148.9, 138.5, 136.3, 133.1, 126.8, 125.1, 118.2, 113.7, 112.8, 110.5; $C_{12}H_6N_2S$ found (calc.): 68.39 (68.55), 3.10 (2.88), 12.76 (13.32), 15.15 (15.25); MS (EI): m/z = 210 (100 %); IR (KBr cm^{-1}) 3097, 2964, 2212, 1602, 1410, 1262, 1096, 1022, 800, 698, 534.

2,2'-bithiophene-5,5'-dicarbonitrile ($BTh(CN)_2$) was synthesized via a Rosenmund-von Braun reaction according to the literature.[2] 2.00 g (6.17 mmol) of 2,2'-bithiophen-5,5'-dibromide and 1.66 g (18.52 mmol) of CuCN was refluxed in 30 mL of DMF for 18 h at 150 °C under nitrogen atmosphere. To the reaction medium, cooled to 60 °C, a solution of 10 g (37 mmol) of $FeCl_3$ x $6H_2O$ dissolved in 23 mL of 2 mol L^{-1} HCl were added at once, and the mixture was stirred for 4 h. Extraction by dichloromethane (3×100 mL) was followed by washing of the combined organic extracts with

2 mol L^{-1} HCl (3×100 mL) then water. The organic layer was dried over $MgSO_4$ and the crude product was recovered *via* evaporation of the solvent. Column chromatography using dichloromethane / ethyl acetate (2:1) yielded 0.360 g of a yellow crystalline product (27 %).
^{1}H NMR (600 Hz, DMSO-d_6) δ (ppm): 8.03 (d, 4.0 Hz, 1H), 7.71 (d, 4.0 Hz,1H); ^{13}C NMR (600 Hz, DMSO-d_6) δ (ppm): 141.7, 140.9, 127.7, 114.3, 109.1; $C_{10}H_4N_2S_2$ found (calc.): 55.50 (55.54), 1.97 (1.86), 12.71 (12.95), 29.72 (29.65); MS (EI): m/z = 216 (100%); IR (KBr cm^{-1}) 3091, 3070, 2214, 1813, 1634, 1426, 1288, 1210, 1154, 1054, 880, 809, 520, 489.

2,2':5',2":5",2"'-quaterthiophene-5,5"'-dicarbonitrile ($QTh(CN)_2$) was synthesized via a palladium-catalyzed C–H arylation according to the literature.[3] 1.00 g (3.08 mmol) of 2,2'-bithiophen-5,5'-dibromide, 2.02 g (18.5 mmol) of 2-thiophencarbonitrile, 286 mg (0.248 mmol) $Pd(PPh_3)_4$, 1.281 g (9.27 mmol) of K_2CO_3, and 0.095 g (0.93 mmol) of pivalic acid were vigorously stirred during 48 h at 110 °C under nitrogen atmosphere. After the mixture was cooled to room temperature, water was added, and the mixture filtered through celite. The celite plug with the residue was washed with 4x50 mL of water and 4x50 mL of diethyl ether (i.e. thoroughly washing of the top layer surface with the poorly soluble crude product, to remove inorganics, 2-thiophenecarbonitrile and the 2,2'-bithiophene-5,5'-dibromide). The crude product was washed down by diethyl ether / tetrahydrofuran (1:1) to separate it from the dark brown residues of the Pd catalyst. After removal of the solvent and thorough washing by 2x50 mL methanol 0.56 g (48 %) of red solid was obtained.
^{1}H NMR (600 MHz, DMSO-d_6) δ(ppm): 7.96 (d, 4.0 Hz, 2H), 7.57 (d, 4.0 Hz, 2H); 7.52 (d, 4.0 Hz, 2H), 7.48 (d, 3.8 Hz, 2H); MS (EI): m/z = 380 (100%); $C_{18}H_8N_2S_4$ found (calc.): 56.80 (56.82), 2.25 (2.12), 5.96 (7.36), 33.61 (33.70); IR (KBr cm^{-1}): 3067, 2960, 2210, 1657, 1536, 1439, 1259, 1039, 851, 793, 540, 494.

Characterization of CTFs

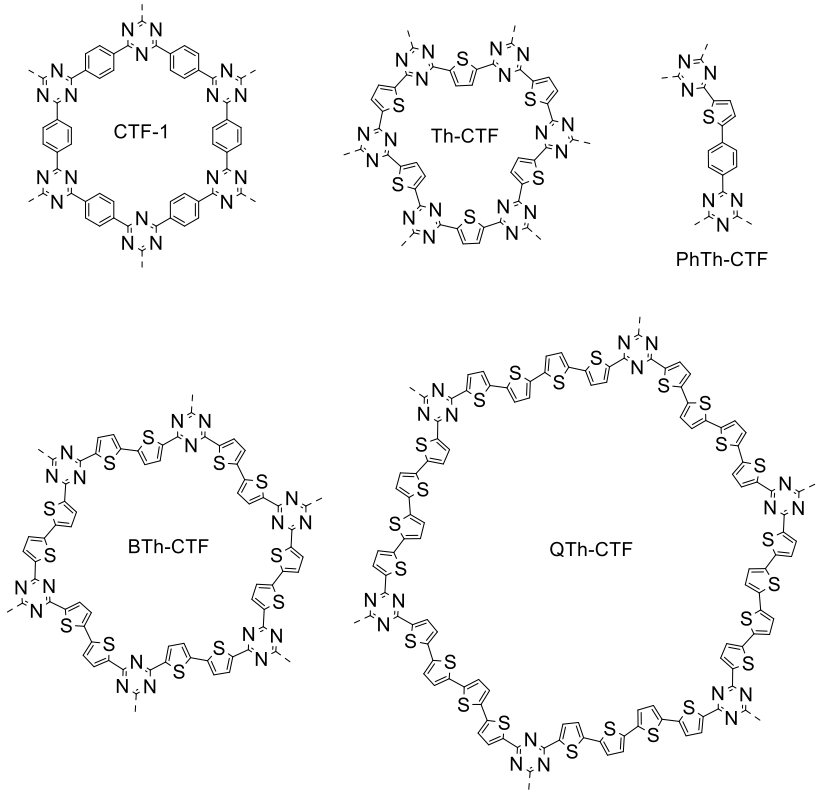

Fig. S2 Idealized illustration of the hexagonal unit in CTFs with phenyl (CTF-1), thiophene (Th-CTF), bithiophene (BTh-CTF) or quaterthiophene (QTh-CTF) linkers between the triazine nodes. The phenylthiophene-linked CTF (PhTh-CTF) is asymmetric and doesn't possess hexagonal units.

Table S1 Parameters for the CTF synthesis**.**

Material	**Step 1 400 °C (h)**	**Step 2 600 °C (h)**	**Precursor (g)**	**Precursor (mmol)**	**$ZnCl_2$ (x10 mmol Precursor) (g)**
CTF-1_400	40	-	0.300	2.341	3.190
CTF-1_600	40	20	0.300	2.341	3.190
Th-CTF_400	40	-	0.300	2.224	3.031
Th-CTF_600	40	20	0.300	2.224	3.031
PhTh-CTF_400	40	-	0.300	1.427	1.944
PhTh-CTF_600	40	20	0.300	1.427	1.944
BTh-CTF_400	40	-	0.300	1.387	1.890
BTh-CTF_600	40	20	0.300	1.387	1.890
QTh-CTF_400	40	-	0.300	0.788	1.075
QTh-CTF_600	40	20	0.300	0.788	1.075

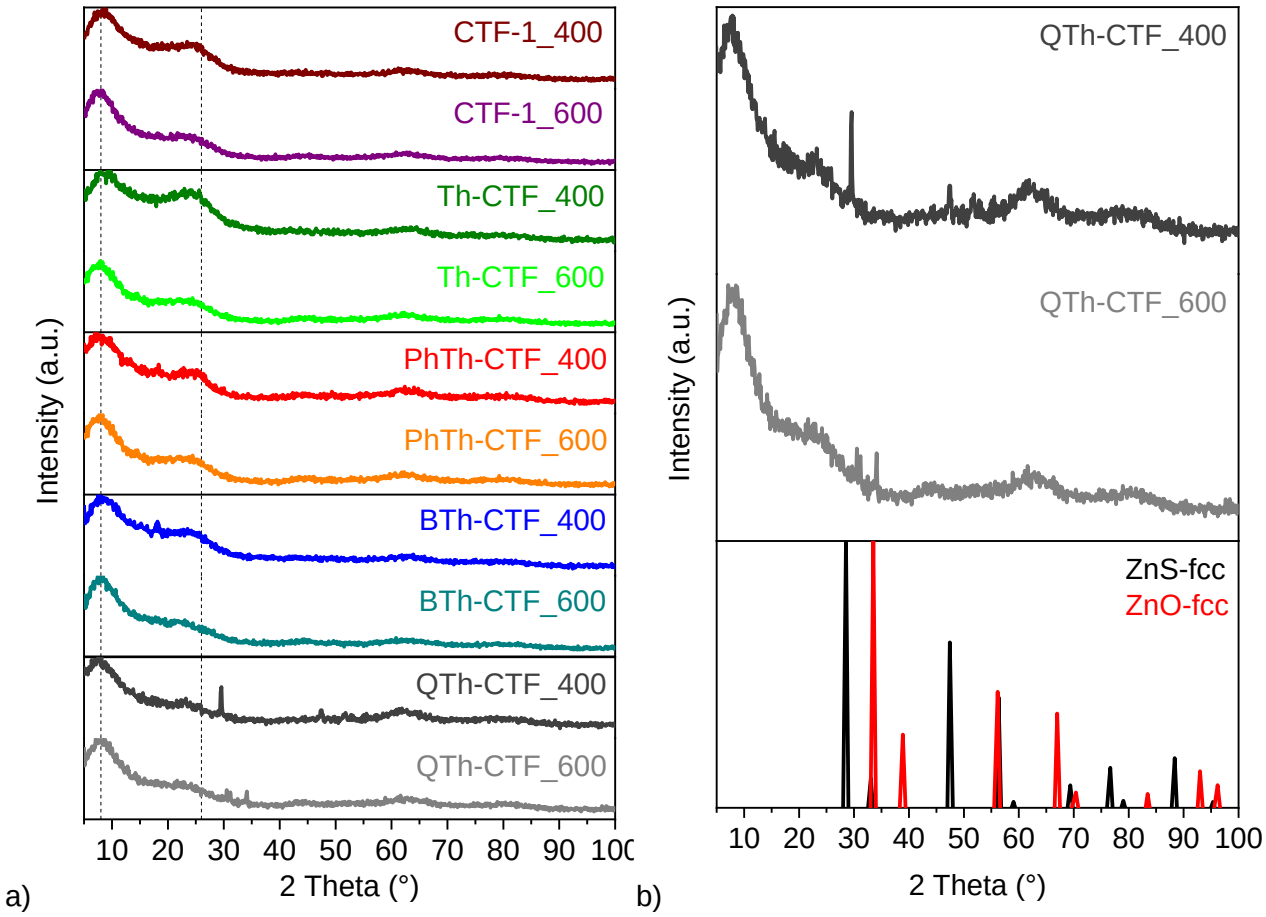

Fig. S3 (a) Powder X-ray diffraction (PXRD) patterns of the synthesized thiophene containing CTFs and the CTF-1 benchmarks. (b) Comparison of the PXRD patterns from the QTh-CTFs samples with the simulated diffractograms of ZnS-fcc (CrOD 1100043) and ZnO-fcc (CrOD 1537875).

Powder patterns in Fig. S3(a) illustrate the absence of crystallinity in the pristine CTFs. This is typical for CTFs which are prepared under the ionothermal synthesis as the high temperatures cause partial decomposition and the formation of defects in the framework. However, broad reflexes were detected at 8° and 26° corresponding to the (100) and (001) planes of layered aromatic sheets.[4-7] Additional reflexes at 28° and 34° in the QTh-CTF samples are assigned to residual amounts of face-centered cubic ZnO and ZnS in the framework (Fig. S3(b)). Minor amounts of Zn are typical for ionothermal synthesized CTFs even after several washing steps.[4] Although these rests were mostly amorphous, the large pores in QTh-CTF appear advantageous for the formation of larger ZnS and ZnO crystallites which are causal for the small reflexes in the diffractograms.

Table S2 Elemental composition of the neat CTFs determined by CHNS analysis.[a]

Material [a,b]	**Carbon (wt%)**	**Hydrogen (wt%)**	**Nitrogen (wt%)**	**Sulfur (wt%)**	**C/(S+N) mass ratio**	**S/N mass ratio**
CTF-1 calc. [a]	*74.99*	*3.15*	*21.86*	-	*3.43*	-
CTF-1_400 (normalized [b])	73.48 (84.70)	2.97 (3.42)	10.30 (11.87)	-	7.13	-
CTF-1_600 (normalized [b])	74.19 (90.07)	1.50 (1.82)	6.68 (8.11)	-	11.11	-
Th-CTF calc. [a]	*53.67*	*1.49*	*20.87*	*23.85*	*1.20*	*1.14*
Th-CTF_400 (normalized [b])	55.19 (62.21)	2.19 (2.47)	17.13 (19.31)	14.21 (16.02)	1.76	0.83
Th-CTF_600 (normalized [b])	63.16 (71.80)	1.68 (1.91)	18.36 (20.87)	4.77 (5.42)	2.73	0.26
PhTh-CTF calc. [a]	*68.55*	*2.88*	*13.32*	*15.25*	*2.40*	*1.14*
PhTh-CTF_400 (normalized [b])	74.64 (91.77)	3.10 (3.81)	1.08 (1.33)	2.51 (3.09)	20.79	2.32
PhTh-CTF_600 (normalized [b])	74.59 (95.02)	1.60 (2.04)	1.54 (1.96)	0.77 (0.98)	32.29	0.50
BTh-CTF calc. [a]	*55.54*	*1.86*	*12.95*	*29.65*	*1.30*	*2.29*
BTh-CTF_400 (normalized [b])	60.99 (67.29)	1.54 (1.70)	7.98 (8.80)	20.13 (22.21)	2.17	2.52
BTh-CTF_600 (normalized [b])	66.77 (81.24)	1.88 (2.29)	7.75 (9.43)	5.79 (7.04)	4.93	0.75
QTh-CTF calc. [a]	*56.82*	*2.12*	*7.36*	*33.70*	*1.38*	*4.58*
QTh-CTF_400 (normalized [b])	66.53 (72.00)	1.59 (1.72)	1.78 (1.93)	22.50 (24.35)	2.74	12.64
QTh-CTF_600 (normalized [b])	77.73 (89.10)	1.47 (1.69)	3.26 (3.74)	4.78 (5.48)	9.67	1.47

[a] Theoretical composition based on the idealized structures of the CTFs (CTF-1: $C_8H_4N_2$; Th-CTF: $C_6H_2N_2S$; PhTh-CTF: $C_{12}H_6N_2S$; BTh-CTF: $C_{10}H_4N_2S_2$; QTh-CTF: $C_{18}H_8N_2S_4$).

[b] The experimental composition wt%(C+H+N+S) does not add up to 100% due to either residual $ZnCl_2$/Zn oxidehydroxide, which cannot be removed completely, incomplete combustion of the CTFs during CHNS analysis and/or the adsorption of moisture from air during CHNS sample preparation.[4,8-12] In order to assess the prospective wt% (C, H, N, S) without this contamination a normalization to 100% has been carried out (entries in parentheses).

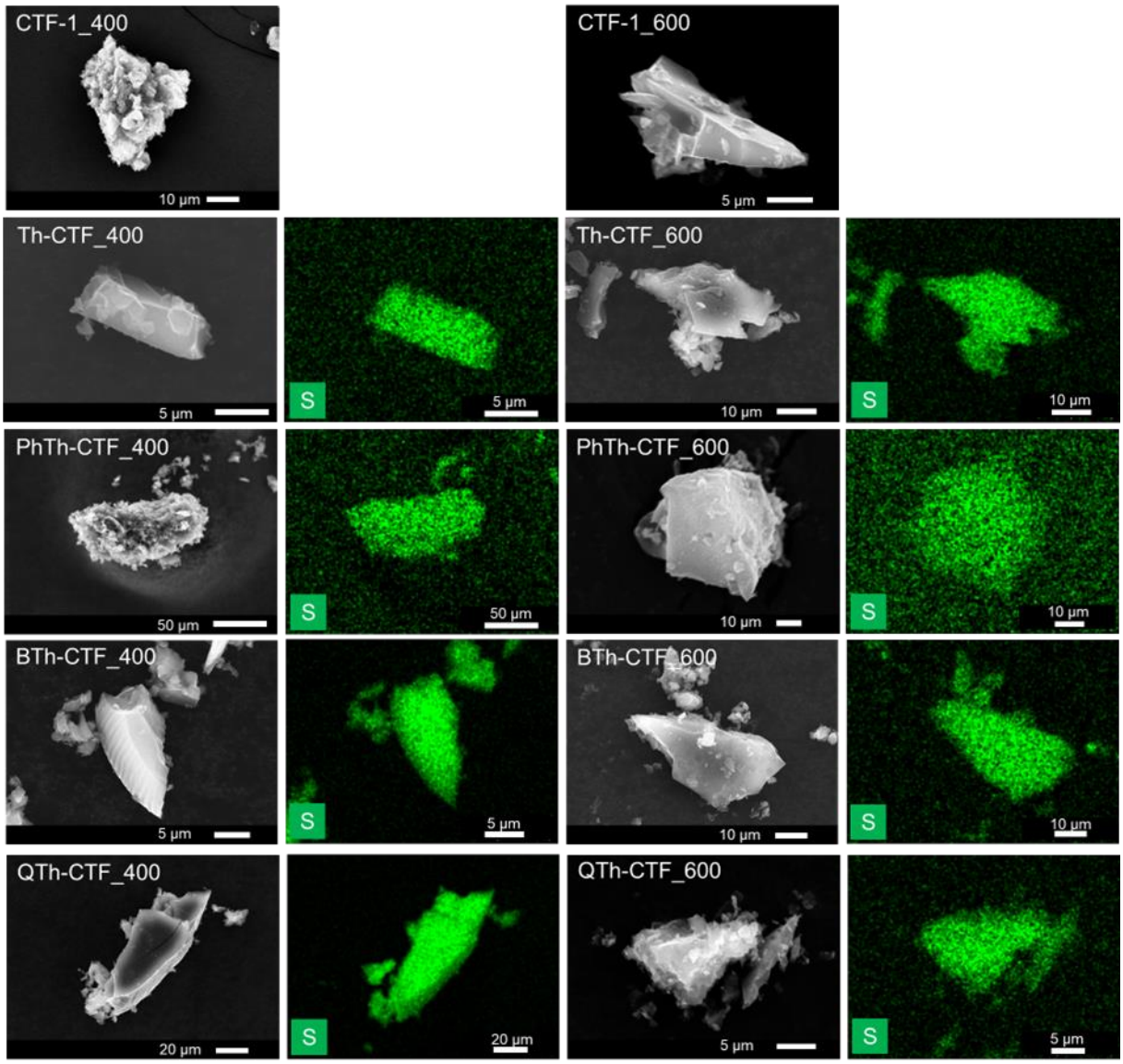

Fig. S4 SEM images and SEM-EDX mapping of sulfur for the CTFs.

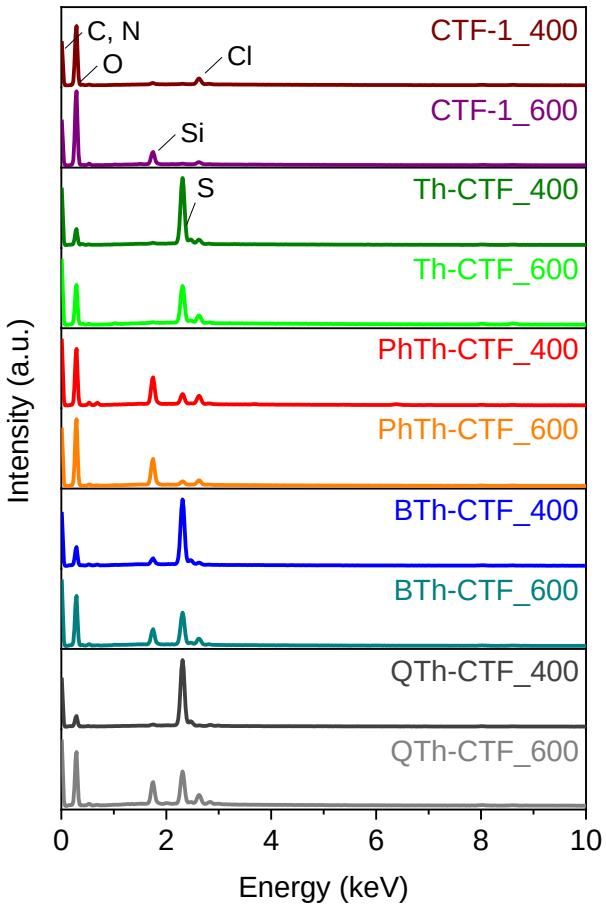

Fig. S5 SEM-EDX spectra of the CTFs.

Fig. S5 depicts the energy dispersive X-ray spectra (SEM-EDX) of the CTF particles. The samples were not gold-sputtered because the CTF ensured sufficient conductivity. This way the sulfur content could be quantified without interference from an otherwise overlapping gold signal. Detected signals belong to C, N, O, Si, S, and Cl. The Si signals in the EDX spectra result from the used glass ware during synthesis or storage and Cl signals from remaining $ZnCl_2$.

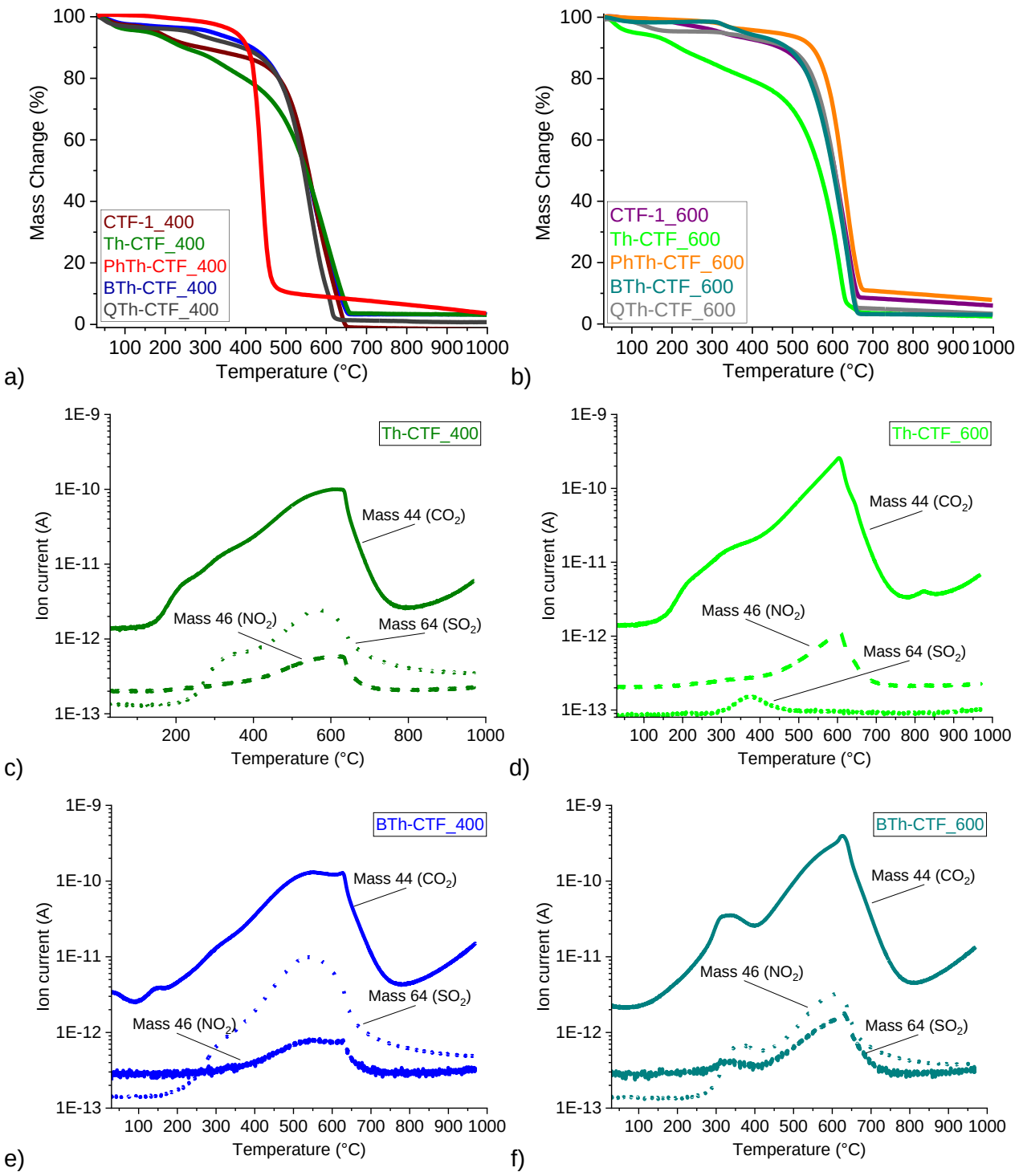

Fig. S6 (a,b) TGA curves for the decomposition of the pure CTFs in synthetic air and (c–f) exemplary mass spectroscopic analysis of gaseous products during decomposition of Th-CTF and BTh-CTF.

Fig. S6a,b shows the curves from thermogravimetric analysis (TGA) of the CTFs under synthetic air and a heating rate of 10 K min^{-1}. Residual masses were below 8°wt% and can result from a slow combustion, as indicated by the still slightly negative slope at 1000 °C, as well as from inorganic impurities, as detected by EDX. The decomposition of CTFs mainly starts at 400 °C demonstrating the high thermal stability of the CTFs.[4,6] However, minor mass losses already happen before 400°C. Only the Th-CTF samples show a continuous high loss of mass already at the beginning. The highest

thermal stability is exhibited by PhTh-CTF_600. Results of mass spectroscopy gas analysis of masses 44 (belonging to CO_2), 46 (belonging to NO_2) and 64 (belonging to SO_2) were illustrated in Fig. S6c-f showing especially the early loss of sulfur from the thiophen units in Th-CTF and BTh-CTF.

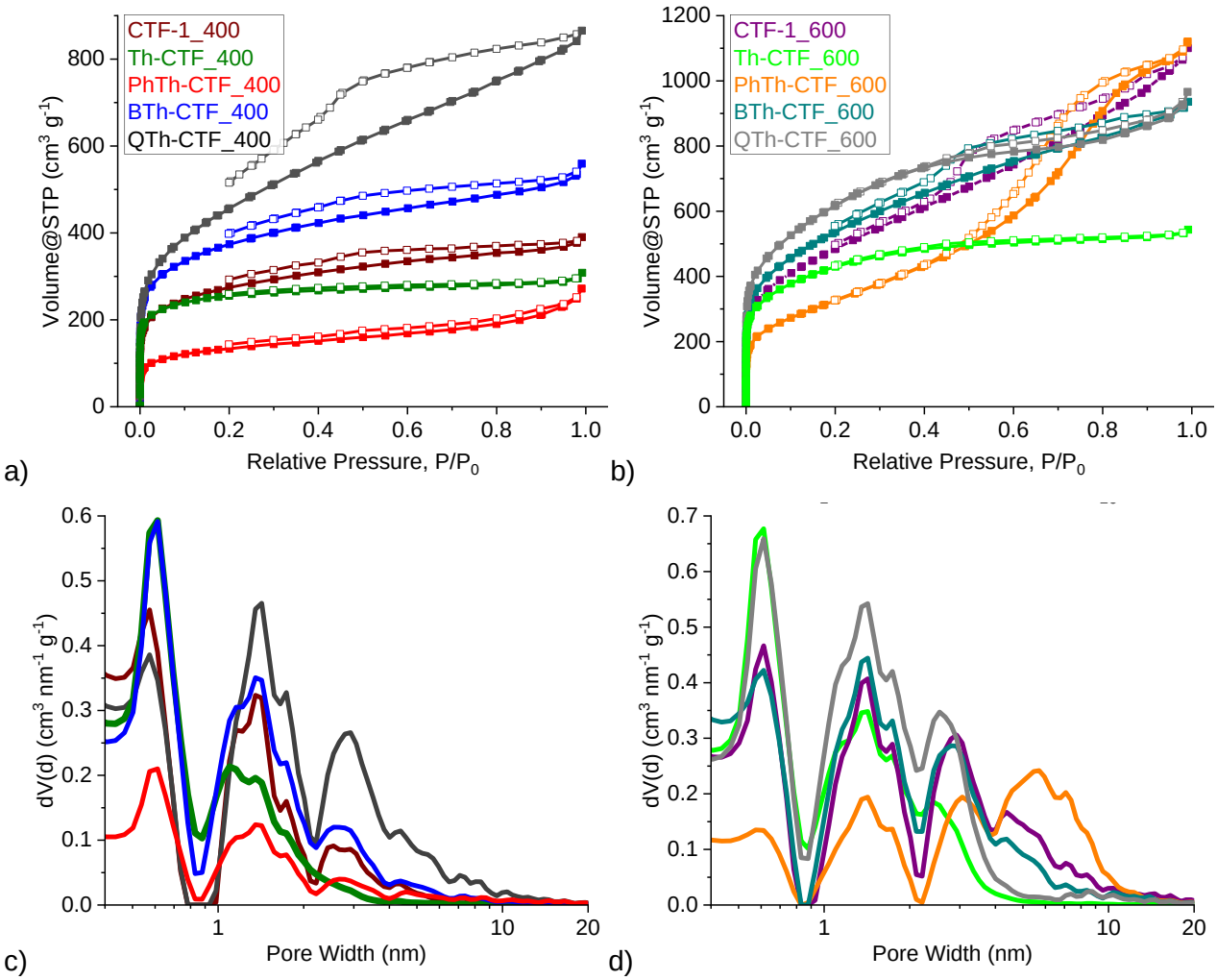

Fig. S7 (a,b) Nitrogen sorption isotherms (adsorption: filled boxes; desorption: empty boxes) and (c,d) pore size distribution curves of the pristine CTFs.

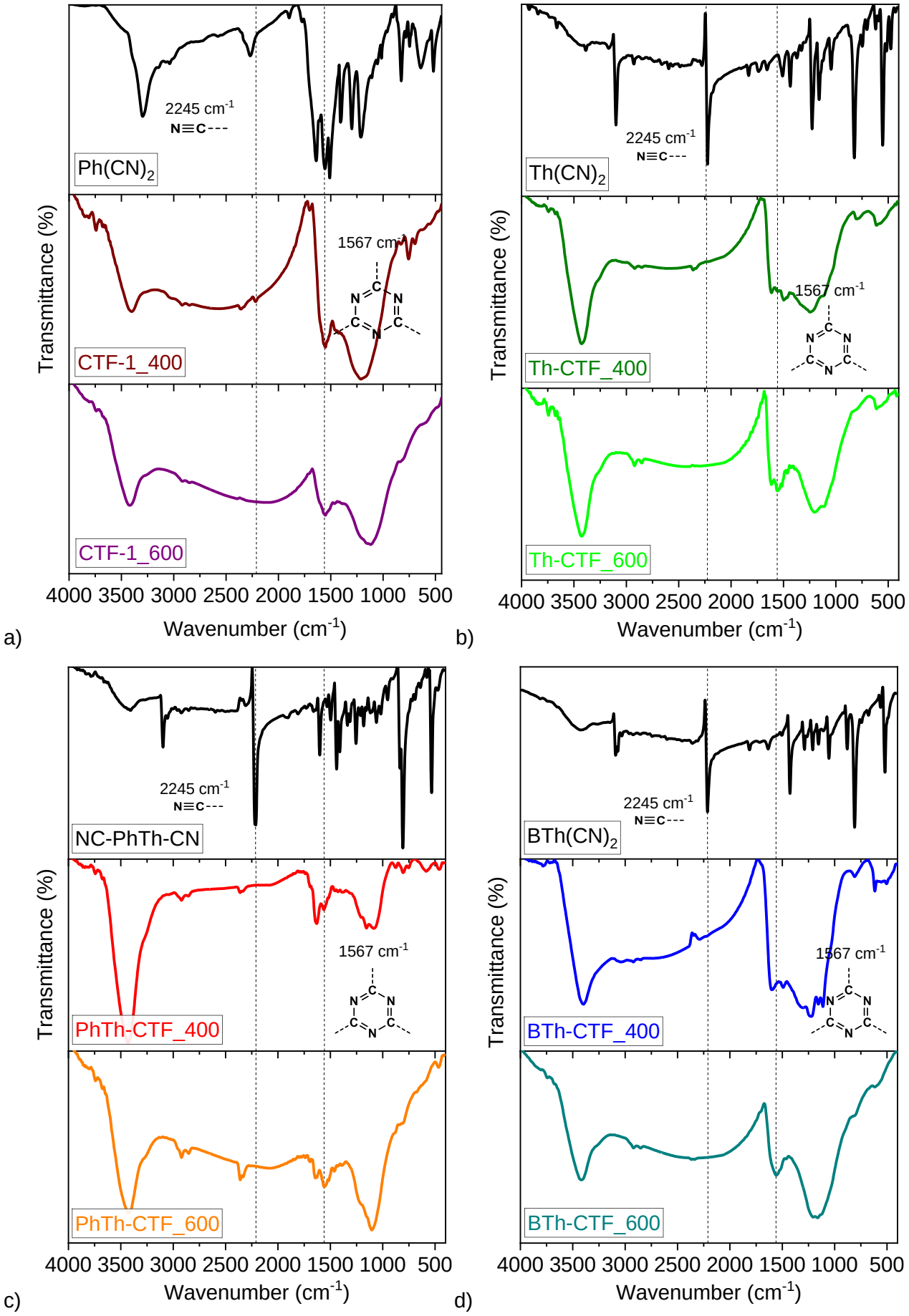
2245 cm-1
N≡C---
Ph(CN)2
1567 cm-1
CTF-1_400
CTF-1_600
Transmittance (%)
4000 3500 3000 2500 2000 1500 1000 500
Wavenumber (cm-1)
a)
2245 cm-1
N≡C---
Th(CN)2
1567 cm-1
Th-CTF_400
Th-CTF_600
Transmittance (%)
4000 3500 3000 2500 2000 1500 1000 500
Wavenumber (cm-1)
b)
2245 cm-1
N≡C---
NC-PhTh-CN
1567 cm-1
PhTh-CTF_400
PhTh-CTF_600
Transmittance (%)
4000 3500 3000 2500 2000 1500 1000 500
Wavenumber (cm-1)
c)
2245 cm-1
N≡C---
BTh(CN)2
1567 cm-1
BTh-CTF_400
BTh-CTF_600
Transmittance (%)
4000 3500 3000 2500 2000 1500 1000 500
Wavenumber (cm-1)
d)

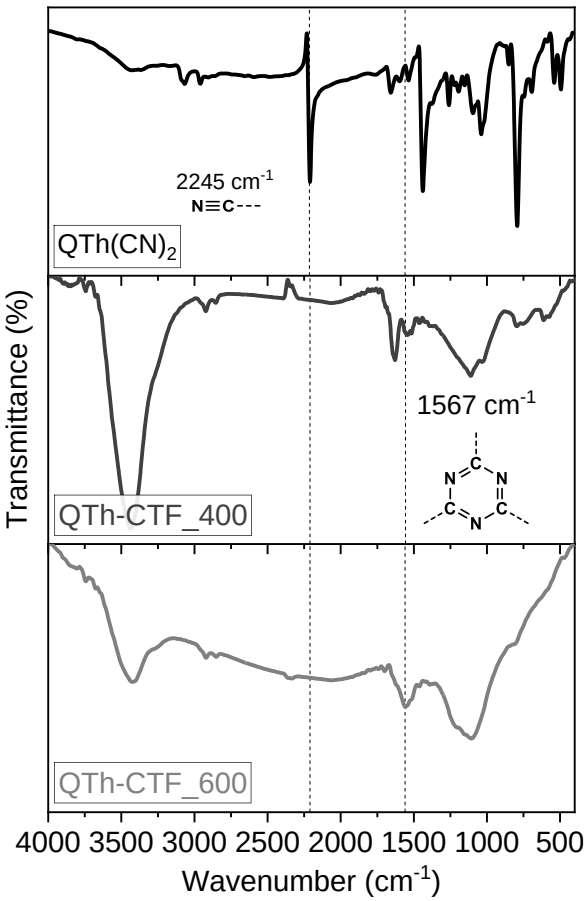

e)

Fig. S8 (a–e) Infrared spectra of the dinitrile CTF precursors and the CTFs.

Characterization of Ru/CTF

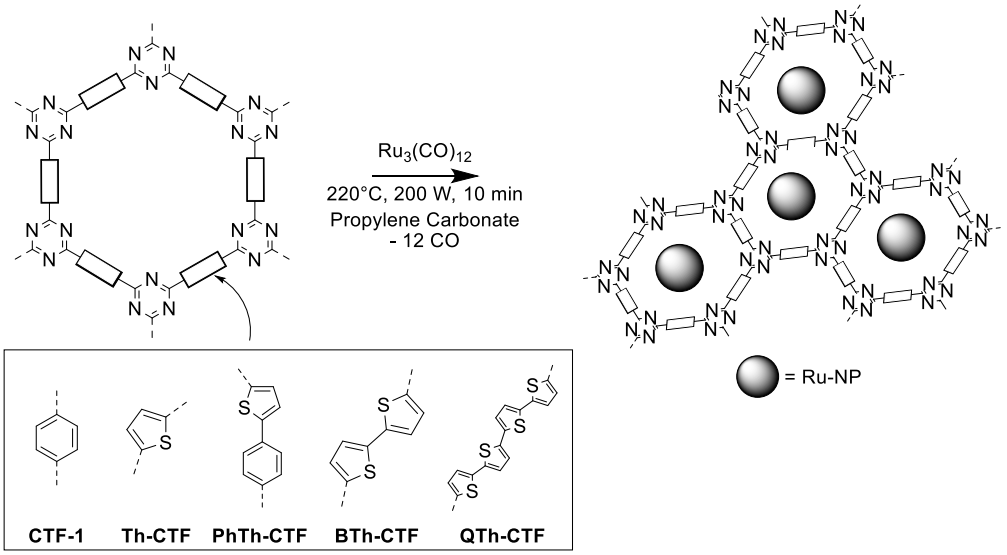

Fig. S9 Microwave assisted synthesis of Ru-NP stabilized on an idealized porous CTF. Bars denote the bridging phenyl (CTF-1), thiophene (Th-CTF), phenylthiophene (PhTh-CTF), bithiophene (BTh-CTF) or quaterthiophene (QTh-CTF) units between the triazine nodes.

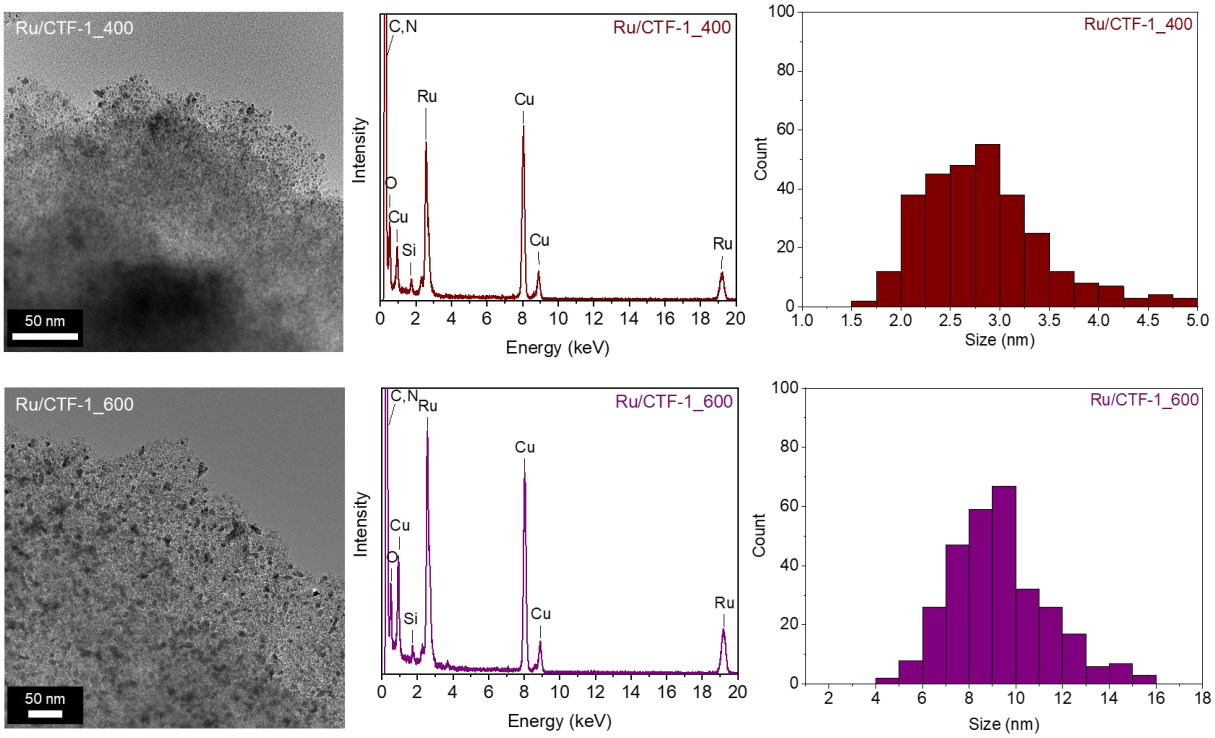

Fig. S10 TEM pictures, TEM-EDX spectra and particle size distribution of Ru/CTF-1_400 (av. 2.8 nm) and Ru/CTF-1_600 (av. 9 nm).

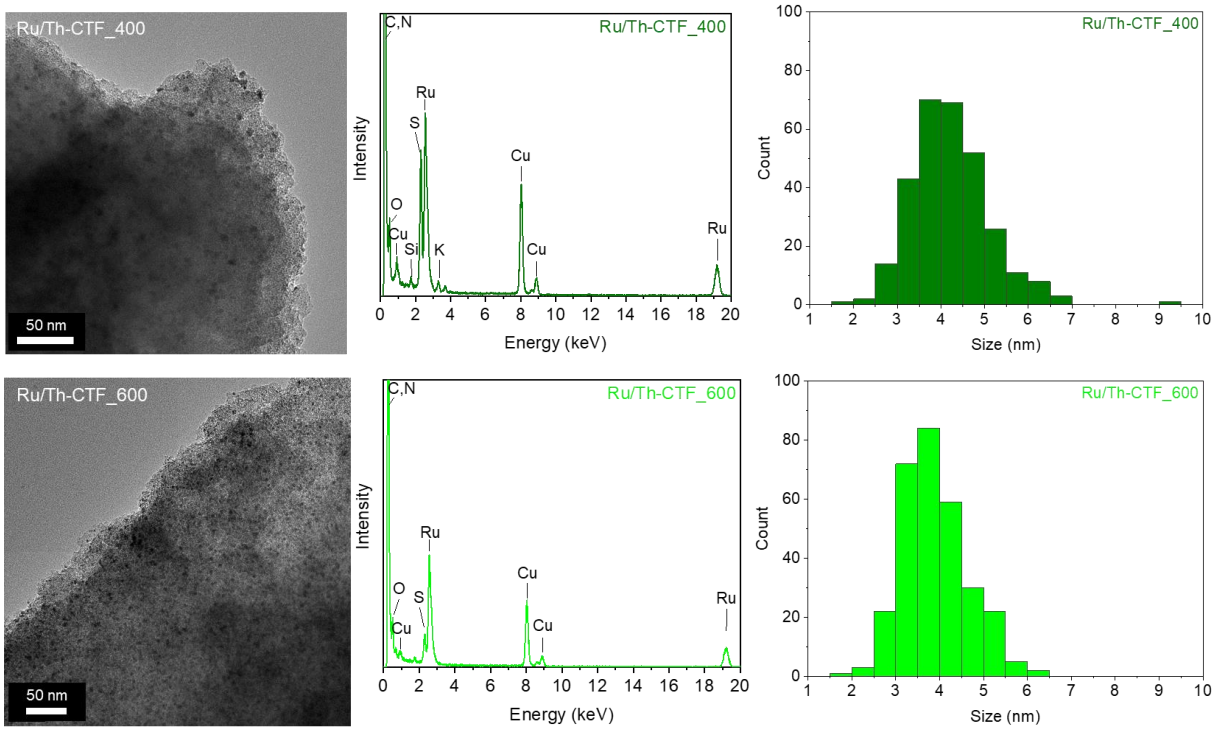

Fig. S11 TEM pictures, TEM-EDX spectra and particle size distribution of Ru/Th-CTF_400 (av. 4.2 nm) and Ru/Th-CTF_600 (av. 3.9 nm).

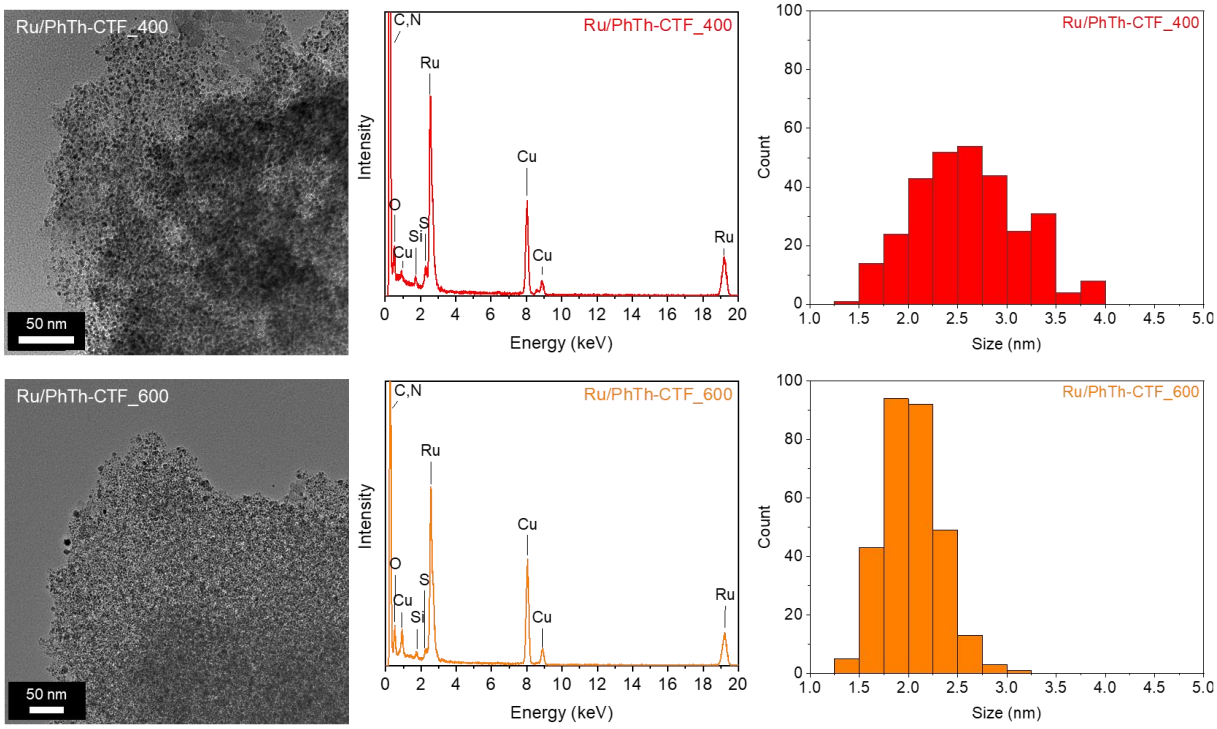

Fig. S12. TEM pictures, TEM-EDX spectra and particle size distribution of Ru/PhTh-CTF_400 (av. 2.6 nm) and Ru/PhTh-CTF_600 (av. 2.0 nm).

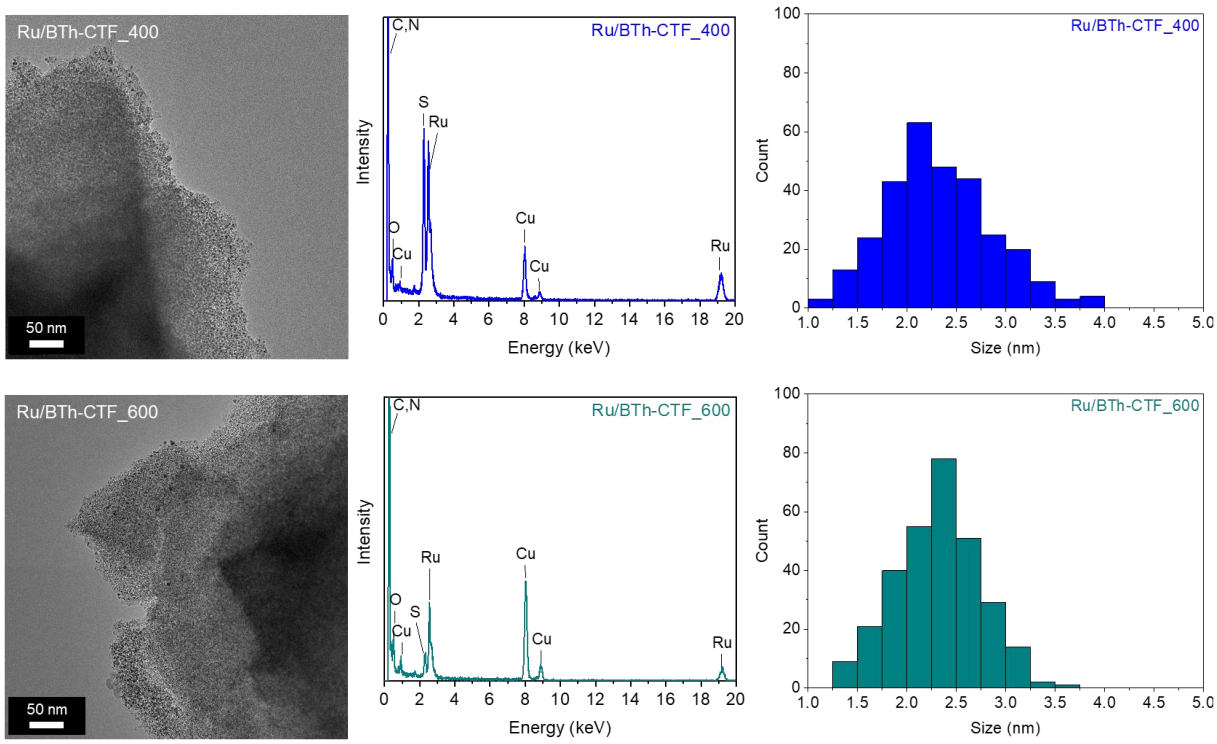

Fig. S13 TEM pictures, TEM-EDX spectra and particle size distribution of Ru/BTh-CTF_400 (av. 2.3 nm) and Ru/BTh-CTF_600 (av. 2.3 nm).

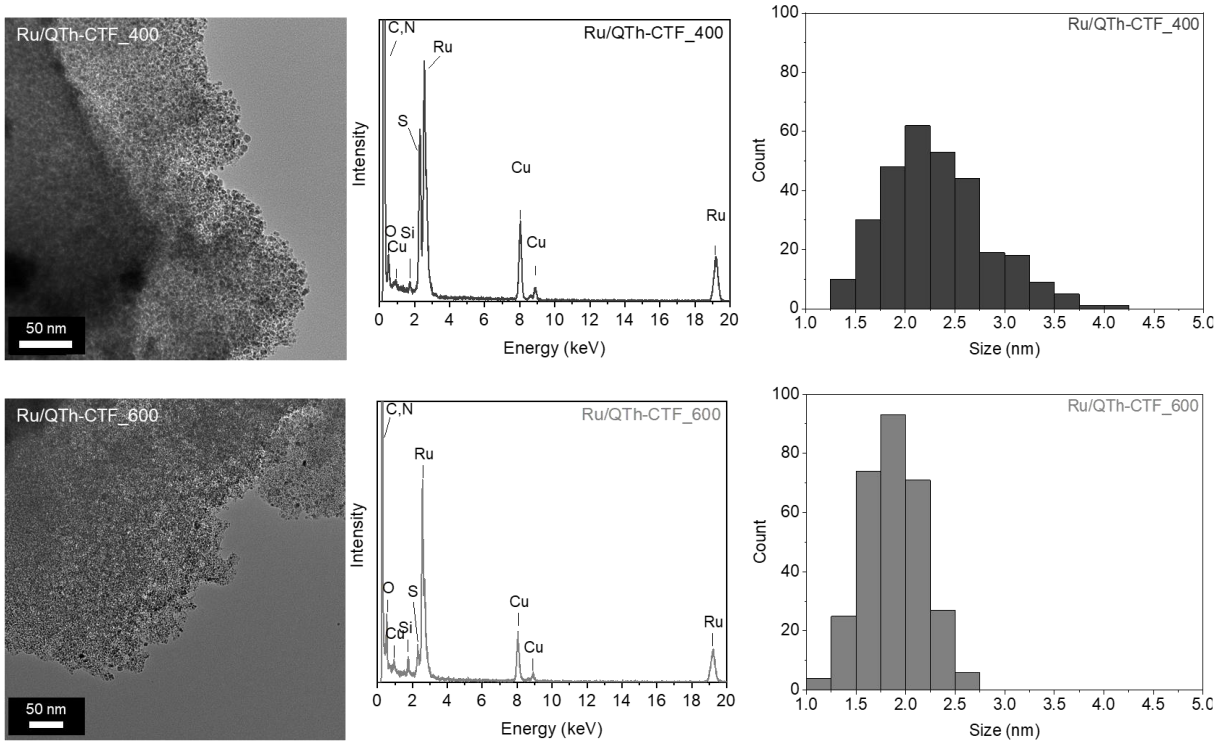

Fig. S14 TEM pictures, TEM-EDX spectra and particle size distribution of Ru/QTh-CTF_400 (av. 2.3 nm) and Ru/QTh-CTF_600 (av. 1.9 nm).

Fig. S10-S14 illustrate supplementary transmission electron microscopy (TEM) images, energy dispersive X-ray spectra (TEM-EDX) and particles size distributions of the Ru-NP decorated CTFs. Average NP sizes from 2 to 9 nm and particles size distributions were manually determined based on 300 particles. The measured NP sizes were approximated as a Gaussian-like distribution for the determination of the average particle size and its standard deviation (cf. Table 2 in the main text). Notably, smaller NPs possess a larger relative number of surface atoms, which has a positive influence on the performance towards electrocatalysis due to more active sites.[13,14] TEM-EDX spectra show the expected signals for Ru and S. Further signals from Si and Cu are observed in the EDX spectra originating from the used glass ware during the synthesis process and from the copper mesh of the TEM grid. The absence of Zn and Cl signals is evidence to an almost complete removal of $ZnCl_2$.

Table S3 Proportions of S, N and Ru species in the Ru/CTF composites determined from XPS fitting.

Material	S species (at%)		N species (at%)				Ru species (at%)	
	$-SO_X$	C-S-C	oxidized	graphitic	pyrrolic	pyridinic	Ru(0)	Ru(n+)
Ru/CTF-1_400	-	-	3.6	55.3	5.0	36.1	58.3	41.7
Ru/CTF-1_600	-	-	15.4	42.3	20.6	21.7	57.6	42.4
Ru/Th-CTF_400	27.0	73.0	3.9	36.2	32.6	27.2	59.8	40.2
Ru/Th-CTF_600	56.2	43.8	12.7	47.8	30.4	9.1	85.0	15.0
Ru/PhTh-CTF_400 [a]	n.d.	n.d.	9.5	46.3	8.5	35.7	69.8	30.2
Ru/PhTh-CTF_600 [a]	n.d.	n.d.	26.0	29.2	8.0	36.8	59.4	40.6
Ru/BTh-CTF_400	33.2	66.8	10.7	44.4	3.0	41.9	69.8	30.2
Ru/BTh-CTF_600	31.9	68.1	14.4	38.7	6.6	40.3	67.3	32.7
Ru/QTh-CTF_400	31.1	68.9	17.2	33.1	2.4	47.3	63.2	36.8
Ru/QTh-CTF_600	39.4	60.6	17.1	42.9	7.0	33.0	58.3	41.7

[a] The amount of ~1 wt% sulfur is below the XPS detection limit.

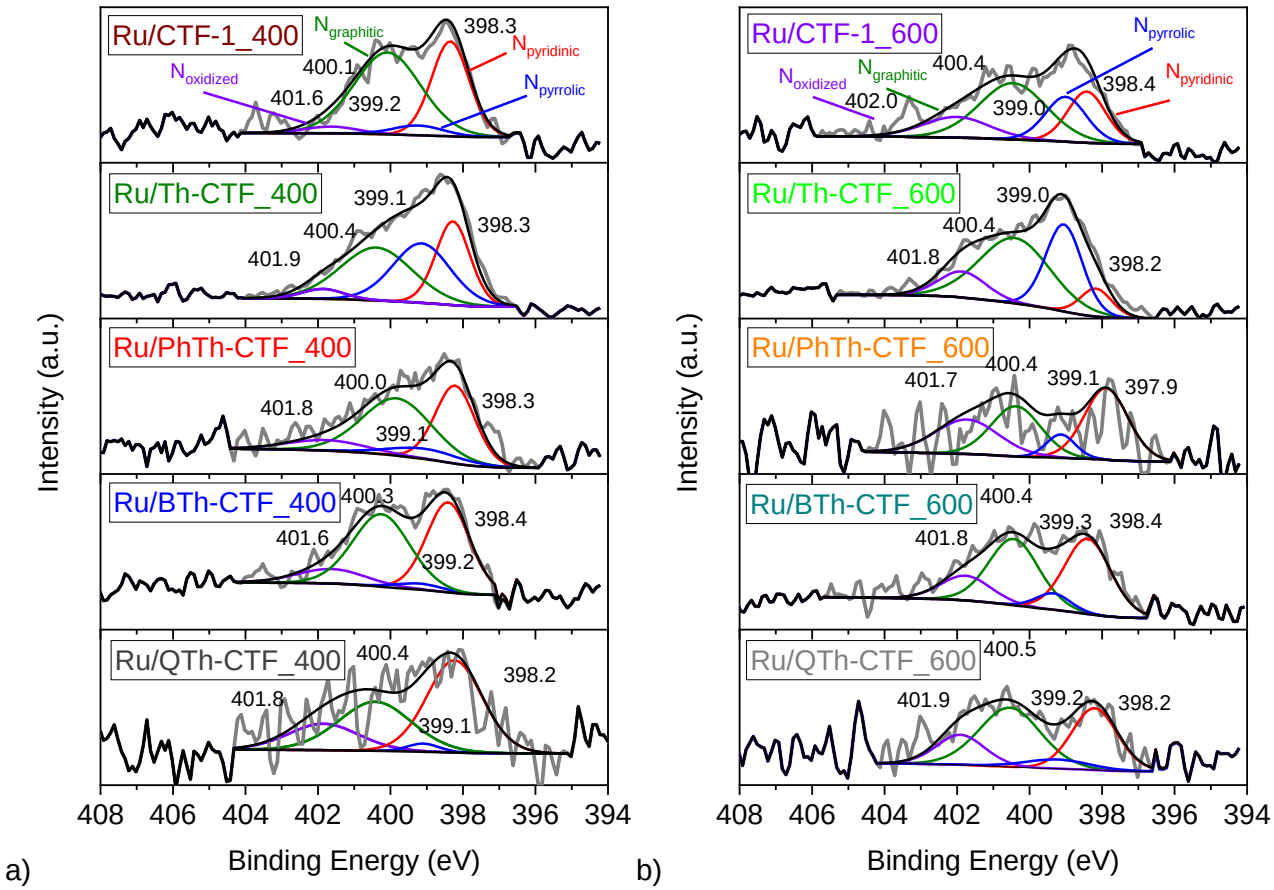

Fig. S15 High resolution X-ray photoelectron spectra of N 1s orbitals from (a) Ru/CTF_400 and (b) Ru/CTF_600 composites. The weak intensities in the N 1s spectra of Ru/PhTh-CTF result from the low amount of nitrogen inside the composite.

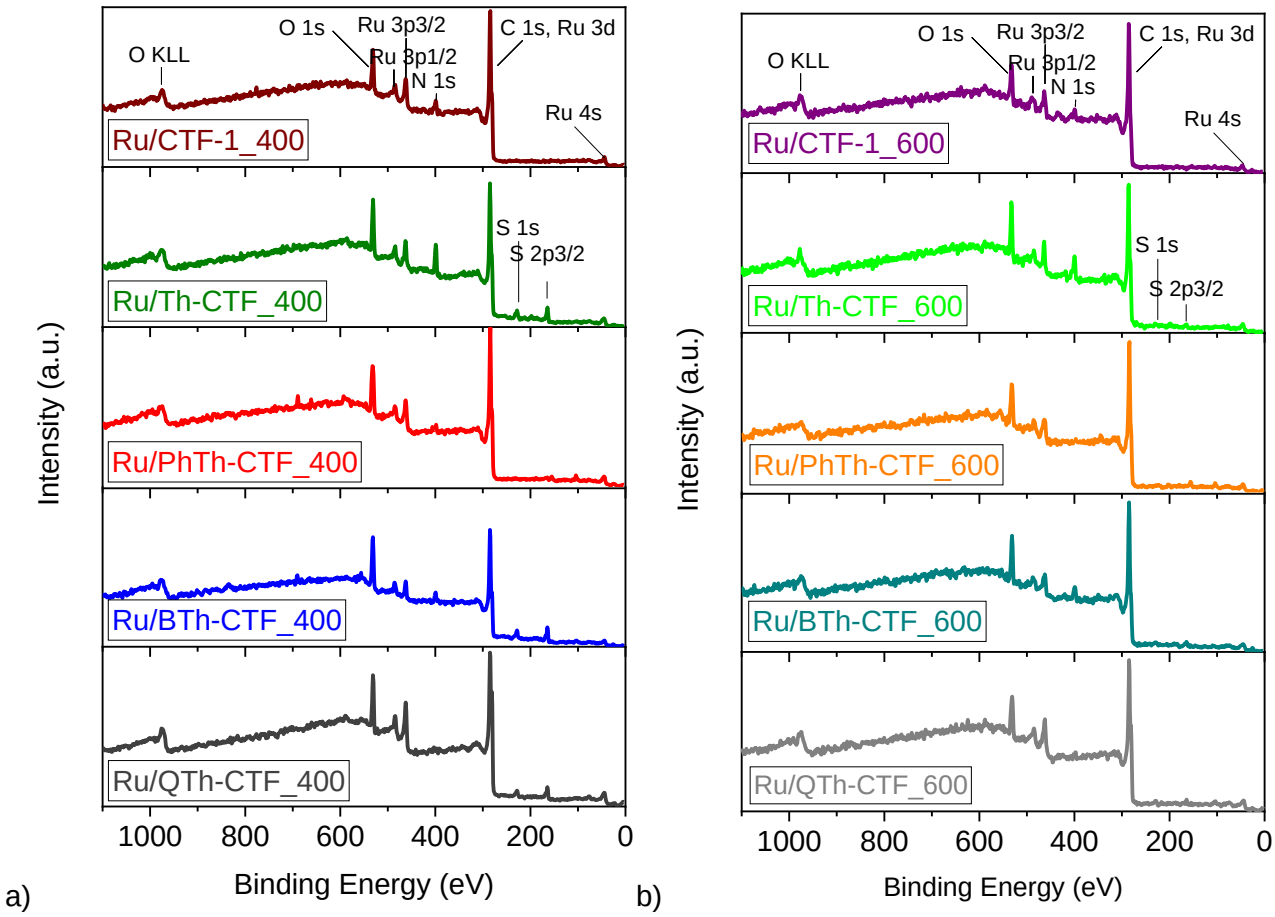

Fig. S16 X-ray photoelectron survey spectra of (a) Ru/CTF_400 and (b) Ru/CTF_600 composites.

Fig. S16 shows the XPS survey spectra of the Ru/CTF_600 samples. Signals can be assigned to Ru, C, N, and S (weakly pronounced signal). The oxygen signal can be attributed to the surface oxidation of the Ru-NPs caused by handling in air.[15,16]

Electrochemical characterization of Ru/CTF

Different Ru:S molar ratios were tested towards the HER by the addition of molecular thiophene onto a dried electrode with Ru/CTF-1_600 as electrocatalysts. For this purpose and in consideration of the Ru loading (10.5 µg (0.104 µmol) Ru on 0.196 cm^{-2} GC), 20.8 µL (0.260 mmol) of thiophene were dissolved in 100 mL of ethanol and subsequently 10 µL (for a Ru:S molar ratio of 1:0.25) of the thiophene/ethanol solution were dispersed on the electrode surface by drop casting. After drying, the electrode was tested in 0.5 mol L^{-1} H_2SO_4 and in 1 mol L^{-1} KOH by linear sweep voltammetry (Fig. S17†). Then, the electrode was carefully cleaned with distilled water and dried. Afterwards, the procedure of successively adding thiophene onto the dried electrode was repeated.

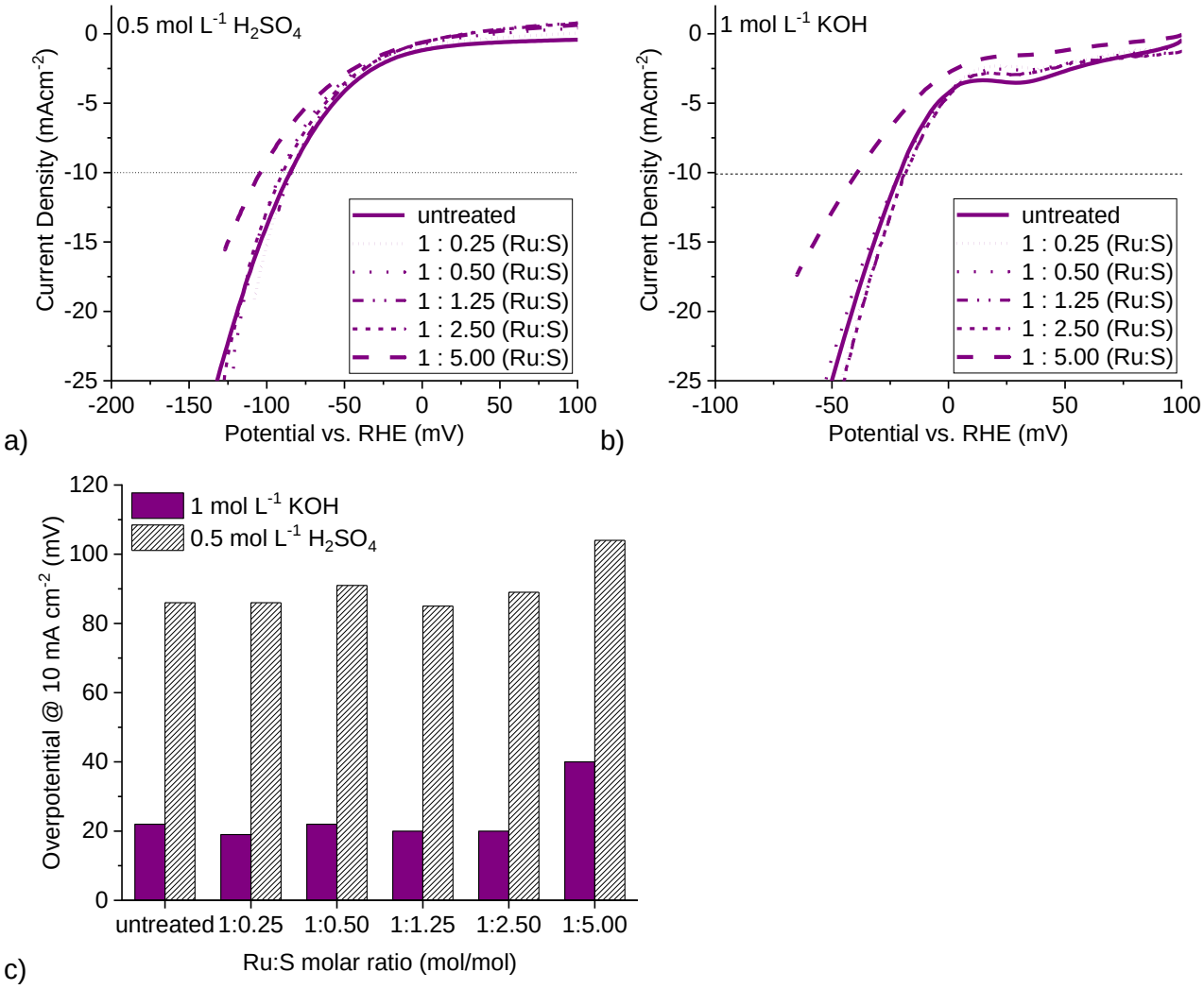

Fig. S17 (a,b) HER LSV polarization curves and (c) overpotentials of Ru/CTF-1_600 with different Ru:S molar ratios by subsequent drop casting of molecular thiophene dissolved in ethanol (c = 2.60 mmol/L) on the electrode surface.

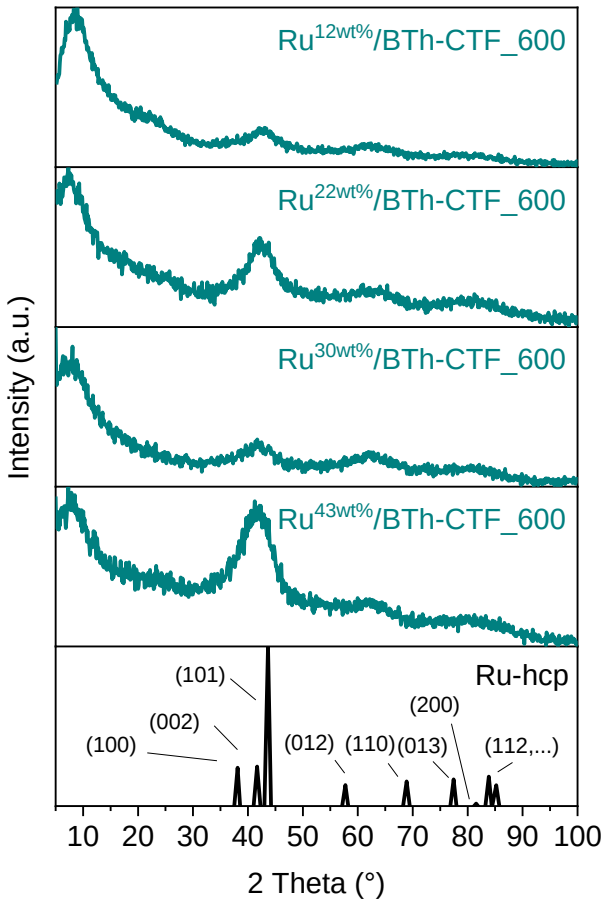

Fig. S18 PXRD patterns of Ru/BTh-CTF_600 with different amounts of Ru. Metal contents were determined by AAS. The determined Ru wt% corresponded to the aimed for 13, 23, 33 or 43 wt% Ru metal contents. The diffractogram of Ru-hcp was simulated from the COD 1512537 entry of the Crystallographic Open Database.

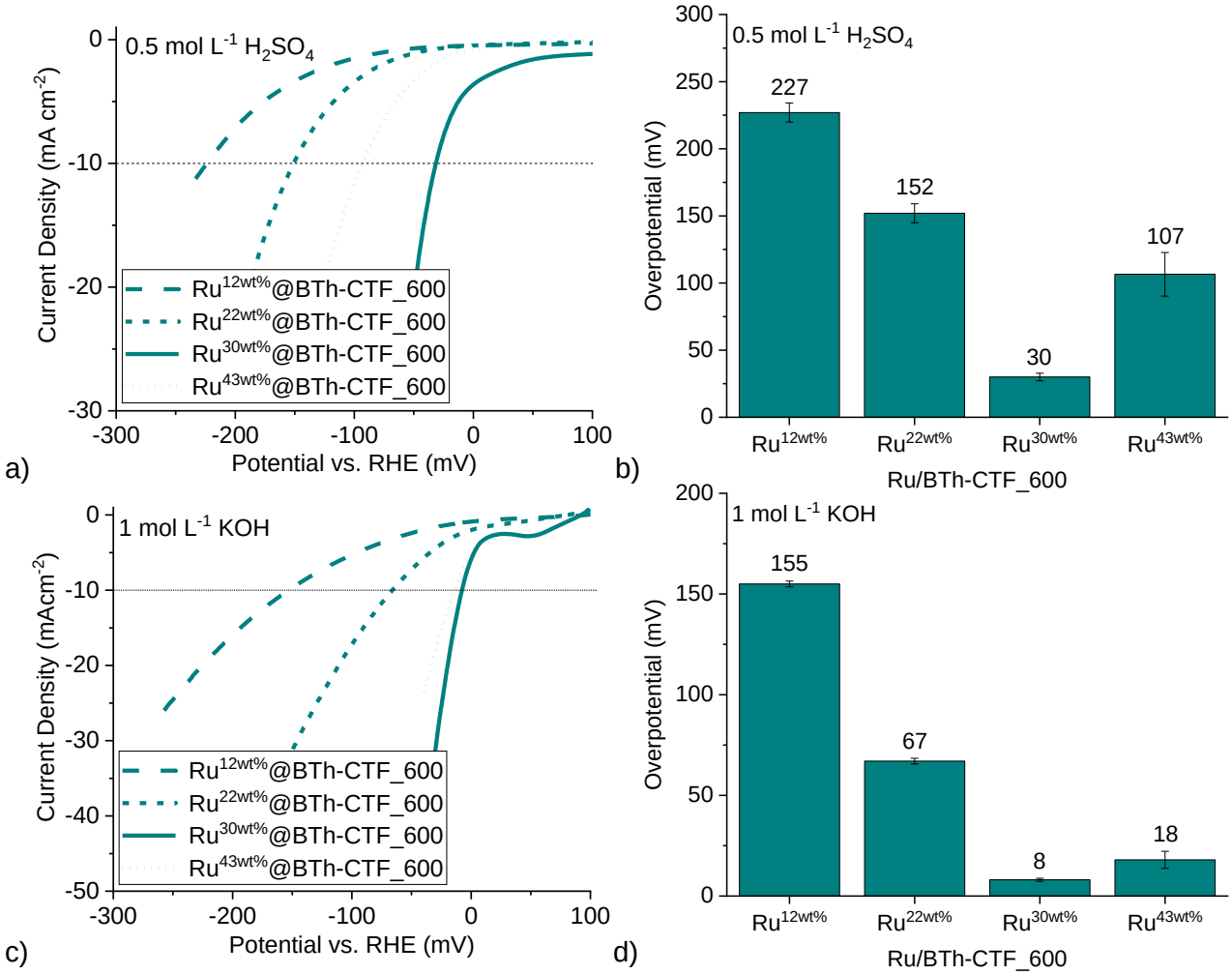

Fig. S19 HER LSV polarization curves and overpotentials of Ru/BTh-CTF_600 with different Ru contents in (a,b) 0.5 mol L^{-1} H_2SO_4 and (c,d) 1 mol L^{-1} KOH.

Fig. S19 illustrates the (a,c) polarization curves and (b,d) overpotentials of the Ru/BTh-CTF_600 sample with different loadings of Ru. The measurements show an optimum in the electrocatalytic performance at 30 wt% Ru. Higher and lower amounts of Ru were disadvantageous in case of Ru/BTh-CTF_600 demonstrating that the amount of metal needs also to be carefully balanced to achieve an optimal electrocatalytic activity.

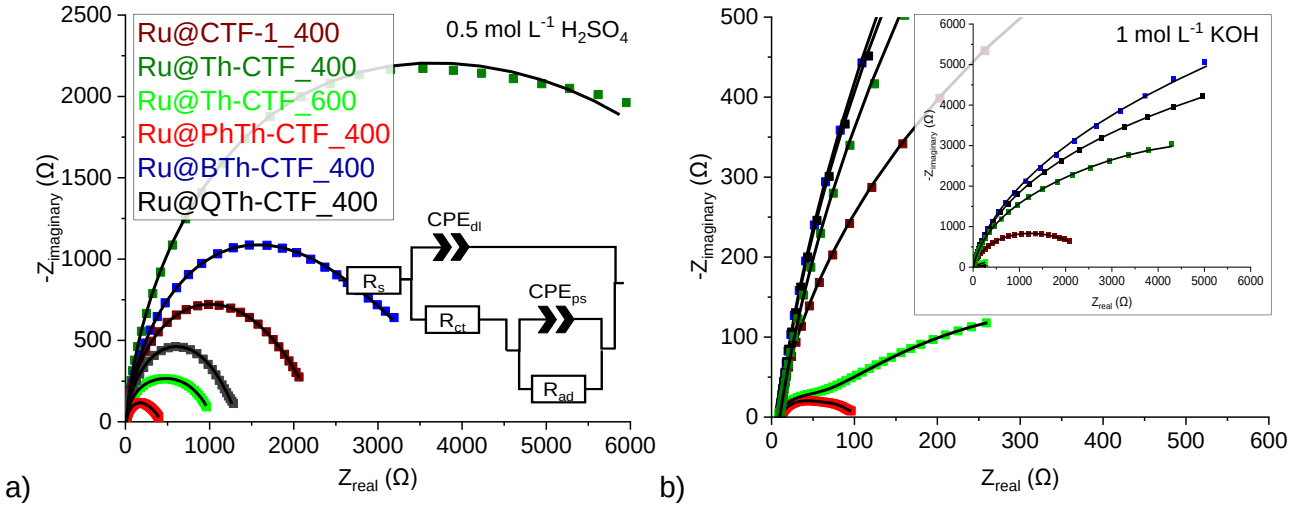

Fig. S20 Nyquist plots of Ru/CTF_400 (a) at −60 mV vs. RHE in 0.5 mol L^{-1} H_2SO_4 and (b) at −20 mV vs. RHE in 1 mol L^{-1} KOH. Fitted EEC models (solid lines) with resistors for the electrolyte resistance, R_S, the charge transfer, R_{ct}, or the hydrogen adsorption, R_{ad}, and constant phase elements assigned to the double layer capacitance, CPE_{dl}, or pseudo capacitance, CPE_{ps}.[17,18]

Nyquist plots of the Ru/CTF_400 composites are illustrated in Fig. S17. By applying a model with two parallel connected time constants (as proposed by Armstrong and Henderson)[18], which takes the charge transfer and the hydrogen adsorption (R_{ad}-CPE_{ps}) into account, resistances for these samples partially reach or exceed 1000°Ω for the adsorption process and the charge transfer.

Table S4 Exchange current densities extracted from the Tafel plots. Estimated charge transfer resistance, hydrogen adsorption resistance and double layer capacitance from the EIS fittings.

Material	**Electrolyte**	**j_0 (mA cm^{-2})**	**R_{ct} (Ω)**	**R_{ad} (Ω)**	**CPE_{dl} (S·s^a)**
Ru/CTF–1_400	H_2SO_4	<0.1	885	1418	<0.001
	KOH	0.2	431	>2000	<0.001
Ru/CTF–1_600	H_2SO_4	1.1	23.1	-	0.002
	KOH	4.3	18.4	-	0.005
Ru/Th–CTF_400	H_2SO_4	<0.1	>2000	>2000	<0.001
	KOH	0.2	>2000	>2000	<0.001
Ru/Th–CTF_600	H_2SO_4	<0.1	826	>2000	<0.001
	KOH	1.2	47.6	656	<0.001
Ru/PhTh–CTF_400	H_2SO_4	0.4	183	235	<0.001
	KOH	3.0	36.2	55.5	<0.001
Ru/PhTh–CTF_600	H_2SO_4	1.0	7.0	-	0.003
	KOH	11.0	5.5	-	0.014
Ru/BTh–CTF_400	H_2SO_4	<0.1	1582	>2000	<0.001
	KOH	<0.1	>2000	>2000	<0.001
Ru/BTh–CTF_600	H_2SO_4	3.0	5.2	-	0.004
	KOH	7.0	9.3	-	0.012
Ru/QTh–CTF_400	H_2SO_4	<0.1	718	636	<0.001
	KOH	<0.1	>2000	>2000	<0.001
Ru/QTh–CTF_600	H_2SO_4	2.0	7.6	-	0.003
	KOH	9.3	8.3	-	0.031

Table S4 summarizes the exchange current densities extracted from the Tafel plots and resistances and capacitances from electrochemical impedance spectroscopy (EIS) fittings. Ru/CTF_600 samples show lower resistances in both electrolytes compared to Ru/CTF_600 samples, also associated with decreasing radii in the Nyquist plots, following a similar trend as in the exchange current densities and overpotentials (cf. Fig. 8 and 9, main text). For some samples resistances exceed 2,000 Ω and double layer capacitances were below 0.001 S s^a in correlation with the sluggish HER performance.

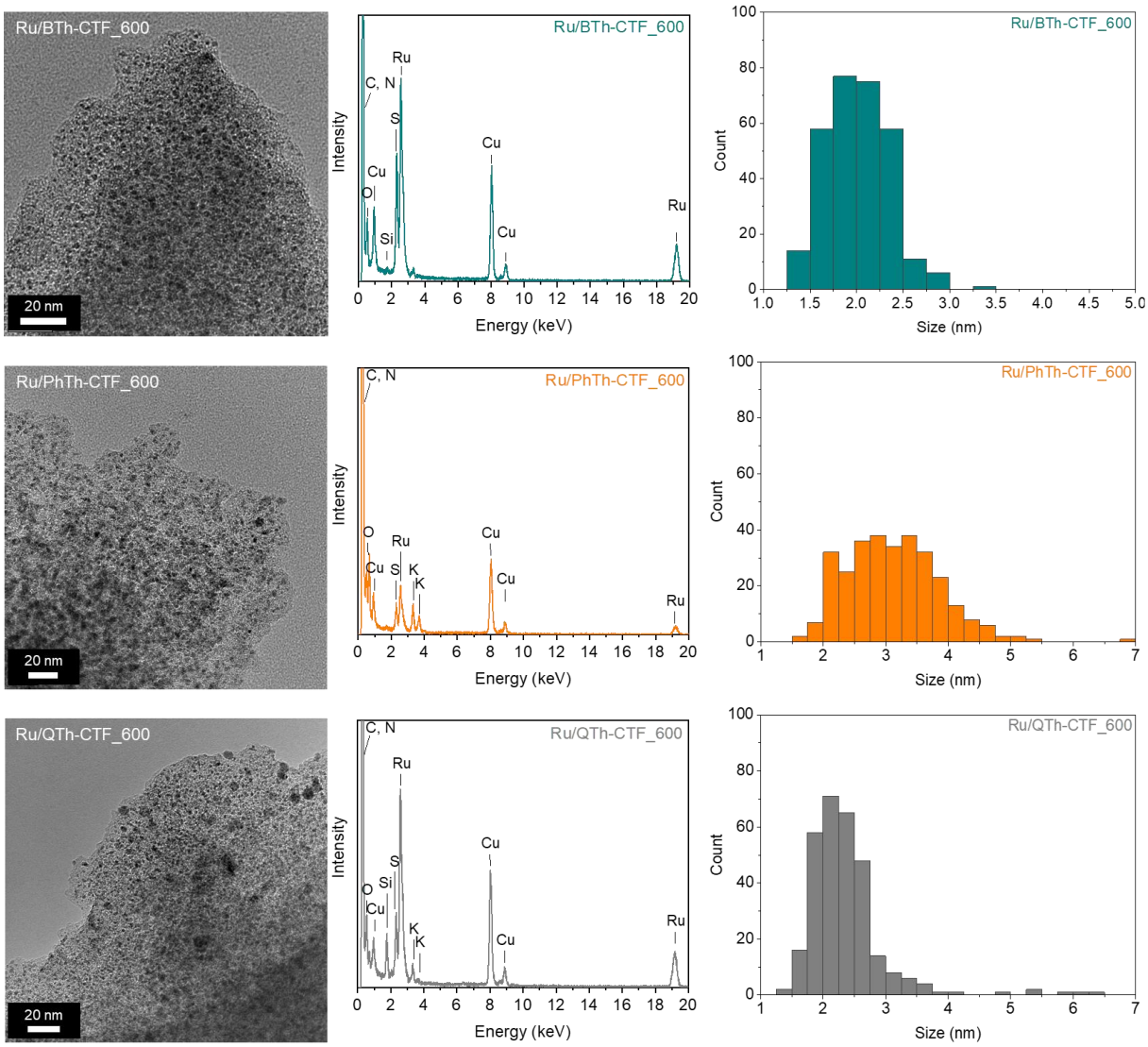

Fig. S21 TEM images, TEM-EDX spectra and particles size distribution after durability test with 2000 CVs of Ru/BTh-CTF600 in 0.5 mol L^{-1} H_2SO_4, of Ru/PhTh-CTF600 in 1 mol L^{-1} KOH, and of Ru/QTh-CTF600 in 1 mol L^{-1} KOH.

TEM images, TEM-EDX spectra and particles size distributions of the Ru/CTF samples with the best performance after the HER stability tests were illustrated in Fig. S18. The element composition of the materials remains preserved. Only potassium persists in Ru/PhTh-CTF_400 and Ru/QTh-CTF_400 originating from the electrolyte. A broadening of the particle size distribution and a shifting to larger particle can be observed compared to the untested samples, whereby the average particle sizes remain unchanged after the CV stability test with 2±1 to 3±1 nm (cf. Table 2, main text).

Comparison of electrocatalysts

Table S5 Performance comparison of electrocatalysts towards HER in acidic and alkaline electrolytes.

Material	**Composition (wt%)** [a]	**Electrolyte**	**Overpotential @ 10 mA cm^{-2} (mV)**	**Tafel slope (mV dec^{-1})**	**Ref.**
Ru/X-CTF (X=Th, PhTh, BTh, QTh) [b]	Ru: 21–33 (AAS) S: 0.7–19.2 (EA) N: 0.9–15.4 (EA)	0.5 mol L^{-1} H_2SO_4	30–436	54–218	this work
		1.0 mol L^{-1} KOH	3–616	39–266	
Ru/CTF-1	Ru: 21, 32 (AAS) N: 6.41, 8.07 (EA)	0.5 mol L^{-1} H_2SO_4	90, 345	92, 110	
		1.0 mol L^{-1} KOH	26, 454	70, 252	
Ru,S(N)-containing materials					
Ru@SGO	Ru: 2.77 (ICP–OES) S: not given	0.5 mol L^{-1} H_2SO_4	69	52	19
		1.0 mol L^{-1} KOH	33	56	
Ru/S-rGO-24	Ru: 10.85 (EDX) S: 1.95 (EDX)	1.0 mol L^{-1} KOH	3	38	20
Ru/N,S-GO	Ru: 7.2 (ICP-AES) S: not given N: not given	1.0 mol L^{-1} KOH	26	30	21
Ru/H-S,N-C	Ru: 16.76 (EDX) S: 2.29 (EDX) N: 1.12 (EDX)	1.0 mol L^{-1} KOH	32	24	22
Ru-N/S-C	Ru: 3 (ICP-AES) S: not given N: not given	1.0 mol L^{-1} KOH	10	36	23
Ru-S/C	Ru: 29.1 (TGA) S: 0.7 (EDX)	1.0 mol L^{-1} KOH	10–114	45–122	24
RuS_x/S-GO	Ru: 55.69 (EDX) S: 44.31 (EDX) Further elements not given	0.5 mol L^{-1} H_2SO_4	31	27	25
		1.0 mol L^{-1} KOH	58	56	
s-RuS_2/S-rGO [c]	Ru: 38 (TGA) S: not given	0.5 mol L^{-1} H_2SO_4	69	64	26
		1.0 mol L^{-1} KOH	25	29	
Ru,N(other)-containing materials					
Ru@C_2N	Ru: 28.7 (TGA)	0.5 mol L^{-1} H_2SO_4	13.5	30	27

	N: not given	1.0 mol L^{-1} KOH	17	38	
Ru@COF-1	Ru: 7.5 (TGA) N: not given	0.5 mol L^{-1} H_2SO_4	200	140	28
Ru/*PC* [d]	Ru: 3.5 (ICP-OES)	1.0 mol L^{-1} KOH	14	44.82	29
Ru-rGO/COF	Ru: not given N: not given	0.5 mol L^{-1} H_2SO_4	132	-	30
		1.0 mol L^{-1} KOH	42	46	
Ru_{1+NPs}/N–C [e]	Ru: 7.57 (ICP-AES) N: not given	0.5 mol L^{-1} H_2SO_4	75	42.7	31
		1.0 mol L^{-1} KOH	39	27.6	
Ru*NCs*/BNG [f]	Ru: 14.25 (TGA) B: 0.85 (at%, XPS) N: 1.38 (at%, XPS)	1.0 mol L^{-1} KOH	14	28.9	32
S-RuP_2/NPC [g]	Ru: 4.8 (ICP-OES) P: 2.05 (at%, XPS) N: 2.2 (at%, XPS)	0.5 mol L^{-1} H_2SO_4	49	50	33
		1.0 mol L^{-1} KOH	19	41	
Metal containing CTFs					
IrOx@DCP-CTF	Ir: 10–20 (AAS) N: 8.6–22.3 (EA)	0.5 mol L^{-1} H_2SO_4	47–368	28–132	16
Pd@DCP-CTF	Pd: 22–41 (AAS) N: 6.4–19.3 (EA)		135–325	78–166	
DCP-CTF@*MC* [h]	*MC*: not given N: 13.44 (XPS)	0.5 mol L^{-1} H_2SO_4	60–397	30.7–90.2	34
BPY-CTF@*MC* [h]	*MC*: not given N: 11.20 (XPS)		117–470	62.0–95.6	
Pt/CTF-1	Pt: not given N: not given	0.5 mol L^{-1} H_2SO_4	111	88	35
Rh/CTF-1	Rh: 4.4 (AAS) N: 14.6 (EA)		58	37	
Ru/D-CTFs-900 [i]	Ru: 4.03 (ICP-AES) N: 16.3 (EA)	1.0 mol L^{-1} KOH	17	32	36

[a] wt% of heteroatoms considering the metal containing composite and normalized EA. [b] Ru-NPs on ionothermal synthesized CTFs with (Th) thiophen, (PhTh) phenylthiophene, (BTh) bithiophene and (QTh) quaterthiophene bridges between the triazine notes. [c] Spherical ruthenium disulfide on S-doped graphene. [d] Ru clusters on porous carbon. [e] Single-atom Ru and Ru-NP anchored on mesoporous N-doped carbon. [f] Ru nanoclusters on B- and N-doped graphene. [g] Self-synthesized RuP_2 on N,P-dual-doped carbon black. [h] Cu, Ni, Co, Pd, and Pt clusters on a 5,5′-dicyano-2,2′-bipyridine and pyridine-2,6-dicarbonitrile based CTF. [i] Ru-NPs decorated on a defective CTF based on the copolymerization of dicyanobenzene and 2,6-dicyanopyridine via a Brønsted acid approach in CH_2Cl_2 and subsequent calcination at 900°C.

References

1 J. Roger, F. Požgan and H. Doucet, *Green Chem.*, 2009, **11**, 425–432. https://doi.org/10.1039/B819912D

2 L. Friedman and H. Shechter, *J. Org. Chem.*, 1961, **26**, 2522–2524. https://doi.org/10.1021/jo01351a092

3 A. D. Rodrigues, N. Marcotte, F. Quignard, S. Deabate, M. Robitzer and D. A. Lerner, *Spectrochim. Acta A Mol. Biomol. Spectrosc.*, 2020, ***227***, 117708. https://doi.org/10.1016/j.saa.2019.117708

4 P. Kuhn, M. Antonietti and A. Thomas, *Angew. Chem. Int. Ed.*, 2008, **47**, 3450–3453. https://doi.org/10.1002/anie.200705710

5 C. Krishnaraj, H. S. Jena, K. Leus and P. Van Der Voort, *Green Chem.*, 2020, **22**, 1038–1071. https://doi.org/10.1039/C9GC03482J

6 Y. Zhang and S. Jin, *Polymers*, 2018, **11**, 31. https://doi.org/10.3390/polym11010031

7 L. Liao, M. Li, Y. Yin, J. Chen, Q. Zhong, R. Du, S. Liu, Y. He, W. Fu and F. Zeng, *ACS Omega*, 2023, **8**, 4527–4542. https://doi.org/10.1021/acsomega.2c06961

8 P. Kuhn, A. Thomas and M. Antonietti, *Macromolecules*, 2009, **42**, 319–326. https://doi.org/10.1021/ma802322j

9 S. Dey, A. Bhunia, D. Esquivel and C. Janiak, *J. Mater. Chem. A*, 2016, **4**, 6259−6263. https://doi.org/10.1039/C6TA00638H

10 S. Dey, A. Bhunia, H. Breitzke, P. B. Groszewicz, G. Buntkowsky and C. Janiak, *J. Mater. Chem. A*, 2017, **5**, 3609−3620. https://doi.org/10.1039/C6TA07076K

11 S. Dey, A. Bhunia, I. Boldog and C. Janiak, *Micropor. Mesopor. Mat.*, 2017, **241**, 303–315. https://doi.org/10.1016/j.micromeso.2016.11.033

12 S. Bügel, Q. D. Hoang, A. Spieß, Y. Sun, S. Xing and C. Janiak, *Membranes*, 2021, **11**, 795. https://doi.org/10.3390/membranes11100795

13 W. Luo, Y. Wang and C. Cheng, *Mater. Today Phys.*, 2020, **15**, 100274. https://doi.org/10.1016/j.mtphys.2020.100274

14 S. Xu, M. Niu, G. Zhao, S. Ming, X. Li, Q. Zhu, L. X. Ding, M. Kim, A. A. Alothman, M. S. S. Mushab and Y. Yamauchi, *Nano Research*, 2023, **16**, 6212–6219. https://doi.org/10.1007/s12274-022-5250-1

15 X. Sun, X. Gao, J. Chen, X. Wang, H. Chang, B. Li, D. Song, J. Li, H. Li and N. Wang, *ACS Appl. Mater. Interfaces*, 2020, **12**, 48591–48597. https://doi.org/10.1021/acsami.0c14170

16 L. Rademacher, T. H. Y. Beglau, T. Heinen, J. Barthel and C. Janiak, *Front. Chem.*, 2022, **10**, 945261. https://doi.org/10.3389/fchem.2022.945261

17 A. Lasia, in *Modern Aspects of Electrochemistry*, eds. B. E. Conway, J. O. Bockris and R. E. White, Springer, Boston, 2002, 32, pp. 143–248. https://doi.org/10.1007/0-306-46916–2_2

18 R. D. Armstrong and M. Henderson, *J. Electroanal. Chem. Interfacial Electrochem.*, 1972, **39**, 81-90. https://doi.org/10.1016/S0022-0728(72)80477-7

19 H. L. Jia, C. L. Guo, R. X. Chen, J. Zhao, R. Liu and M. Y. Guan, *New J. Chem.*, 2021, **45**, 22378–22385. https://doi.org/10.1039/D1NJ04765E

20 X. Sun, X. Gao, J. Chen, X. Wang, H. Chang, B. Li, D. Song, J. Li, H. Li and N. Wang, *ACS Appl. Mater. Interfaces*, 2020, **12**, 48591–48597. https://doi.org/10.1021/acsami.0c14170

21 M. J. Wang, M. Ji, X. Zheng, C. Jiang, H. Zhao, Z. X. Mao, M. Zhang, C. Zhu and J. Xu, *Appl. Surf. Sci.*, 2021, **551**, 148742. https://doi.org/10.1016/j.apsusc.2020.148742

22 Y. Wang, W. Luo, H. Li and C. Cheng, *Nanoscale Adv.*, 2021, **3**, 5068–5074. https://doi.org/10.1039/D1NA00424G

23 C. F. Li, J. W. Zhao, L. J. Xie, Y. Wang, H. B. Tang, L. R. Zheng and G. R. Li, *J. Mater. Chem. A*, 2021, **9**, 12659–12669. https://doi.org/10.1039/D1TA02568F

24 C. Ling, H. B. Li, C. Z. Yuan, Z. Yang, H. B. Chong, X. J. Qian, X. J. Lu, T. Y. Cheang and A. W. Xu, *Catal. Sci. Technol.*, 2021, **11**, 3865–3872. https://doi.org/10.1039/D1CY00621E

25 P. Li, X. Duan, S. Wang, L. Zheng, Y. Li, H. Duan, Y. Kuang and X. Sun, *Small*, 2019, **15**, 1904043. https://doi.org/10.1002/smll.201904043

26 J. Yu, Y. Guo, S. Miao, M. Ni, W. Zhou, Z. Shao, *ACS Appl. Mater. Interfaces*, 2018, **10**, 34098–34107. https://doi.org/10.1021/acsami.8b08239

27 J. Mahmood, F. Li, S. M. Jung, M. S. Okyay, I. Ahmad, S. J. Kim, N. Park, H. Y. Joeng and J. B. Baek, *Nat. Nanotechnol.*, 2017, **12**, 441–446. https://doi.org/10.1038/nnano.2016.304

28 Y. Zhao, Y. Liang, D. Wu, H. Tian, T. Xia, W. Wang, W. Xie, X.-M. Hu and Q. Chen, *Small*, 2022, **18**, 2107750. https://doi.org/10.1002/smll.202107750

29 M. Duan, T. Shu, J. Li, D. Zhang, L. Y. Gan, K. X. Yao and Q. Yuan, *Nano Res.*, 2023, **16**, 8836–8844. https://doi.org/10.1007/s12274-023-5558-5

30 Q. Zhao, S. Chen, H. Ren, C. Chen, W. Yang, *Ind. Eng. Chem. Res.*, 2021, **60**, 11070–11078. https://doi.org/10.1021/acs.iecr.1c01251

31 S. Wang, M. Wang, Z. Liu, S. Liu, Y. Chen, M. Li, H. Zhang, Q. Wu, J. Guo, X. Feng, Z. Chen and Y. Pan, *ACS Appl. Mater. Interfaces*, 2022, **14**, 15250–15258. https://doi.org/10.1021/acsami.2c00652

32 S. Ye, F. Luo, T. Xu, P. Zhang, H. Shi, S. Qin, J. Wu, C. He, X. Ouyang, Q. Zhang, J. Liu and X. Sun, *Nano Energy*, 2020, **68**, 104301. https://doi.org/10.1016/j.nanoen.2019.104301

33 Q. Luo, C. Xu, Q. Chen, J. Wu, Y. Wang, Y. Zhang and G. Fan, *Int. J. Hydrog. Energy*, 2019, **44**, 25632–25641. https://doi.org/10.1016/j.ijhydene.2019.08.028

34 B. Zhang, Y. Zhang, M. Hou, W. Wang, S. Hu, W. Cen, X. Cao, S. Qiao and B. H. Han, *J. Mater. Chem. A*, 2021, **9**, 10146–10159. https://doi.org/10.1039/D1TA00589H

35 M. Siebels, C. Schlüsener, J. Thomas, Y. X. Xiao, X. Y. Yang and C. Janiak, *J. Mater. Chem. A*, 2019, **7**, 11934–11943. https://doi.org/10.1039/C8TA12353E

36 X. Gao, Y. J. Gao, S. Q. Li, J. Yang, G. L. Zhuang, S. W. Deng, Z. H. Yao, X. Zhong, Z. Z. Wei, J. G. Wang, *J. Energy Chem.*, 2020, **50**, 135-142. https://doi.org/10.1016/j.jechem.2020.03.022